

¹ Defocus Corrected Large Area Cryo-EM (DeCo-LACE) for Label-Free
² Detection of Molecules across Entire Cell Sections

³

⁴ This manuscript (permalink) was automatically generated from jojoelfe/deco_lace_template_matching_manuscript@26bf17f
⁵ on May 27, 2022.

⁶ **Authors**

- ⁷ • **Johannes Elferich**  0000-0002-9911-706X ·  jojoelfe RNA Therapeutic Institute, UMass Chan Medical
⁸ School; HHMI
- ⁹ • **Giulia Schiroli** None
- ¹⁰ • **David Scadden** None
- ¹¹ • **Nikolaus Grigorieff**  0000-0002-1506-909X ·  nikogrigorieff RNA Therapeutic Institute, UMass Chan
¹² Medical School; HHMI

¹³ **Abstract**

¹⁴ Localization of biomolecules inside a cell is an important goal of biological imaging. Fluorescence microscopy
¹⁵ can localize biomolecules inside whole cells and tissues, but its ability to count biomolecules and accuracy of the
¹⁶ spatial coordinates is limited by the wavelength of visible light. Cryo-electron microscopy (cryo-EM) provides highly
¹⁷ accurate position and orientation information of biomolecules but is often confined to small fields of view inside
¹⁸ a cell, limiting biological context. In this study we use a new data-acquisition scheme called “Defocus-Corrected
¹⁹ Large-Area cryo-EM” (DeCo-LACE) to collect high-resolution cryo-EM data over entire sections (100 – 200 nm
²⁰ thick lamellae) of neutrophil-like mouse cells, representing 1-2% of the total cellular volume. We use 2D template
²¹ matching (2DTM) to determine localization and orientation of the large ribosomal subunit in these sections. These
²² data provide “maps” of translational activity across sections of mammalian cells. This new high-throughput cryo-
²³ EM data collection approach together with 2DTM will advance visual proteomics and complement other single-cell
²⁴ “omics” techniques, such as flow-cytometry and single-cell sequencing.

25 **Introduction**

26 A major goal in understanding cellular processes is the knowledge of the amounts, location, interactions, and
27 conformations of biomolecules inside the cell. This knowledge can be obtained by approaches broadly divided into
28 label- and label-free techniques. In label-dependent techniques a probe is physically attached to a molecule of
29 interest that is able to be detected by its strong signal, such as a fluorescent molecule. In label-free techniques,
30 the physical properties of molecules themselves are used for detection. An example for this is proteomics using
31 mass-spectrometry [1]. The advantage of label-free techniques is that they can provide information over thousands
32 of molecules, while label-dependent techniques offer highly specific information for a few molecules. Especially
33 spatial information can often only be achieved using label-dependent techniques, such as fluorescence microscopy
34 [2].

35 Cryo-electron microscopy (cryo-EM) has the potential to directly visualize the arrangement of atoms that compose
36 biomolecules inside of cells, thereby allowing label-free detection with high spatial accuracy. This has been called
37 “visual proteomics” [3]. Since cryo-EM requires thin samples (<500nm), imaging of biomolecules inside cells is
38 restricted to small organisms, thin regions of cells, or samples that have been suitably thinned. Thinning can
39 be achieved either by mechanical sectioning [4] or by milling using a focused ion beam (FIB) [5]. This complex
40 workflow leads to a low throughput of cryo-EM imaging of cells and is further limited by the fact that at the required
41 magnifications, typical fields of view (FOV) are very small compared to mammalian cells, and the FOV achieved
42 by label-dependent techniques such as fluorescence light microscopy. The predominant cryo-EM technique for
43 the localization of biomolecules of defined size and shape inside cells is cryo-electron tomography [6]. However, the
44 requirement of a tilt series at every imaged location and subsequent image alignment, severely limits the throughput
45 for molecular localization.

46 An alternative approach is to identify molecules by their structural “fingerprint” in single projection using “2D
47 template-matching” (2DTM) [7,8,9]. In this method, a 3D model of a biomolecule is used as a template to find 2D
48 projections that match the molecules visible in the electron micrographs. This method requires a projection search
49 on a fine angular grid, and the projections are used to find local cross-correlation peaks with the micrograph. Since
50 the location of a biomolecule in the z-direction causes predictable aberrations to the projection image, this method
51 can be used to calculate complete 3D coordinates and orientations of a biomolecule in a cellular sample [8].

52 Here we apply 2DTM of the ribosome large subunit (LSU) to cryo-FIB milled neutrophil-like murine cells [10].
53 We chose these cells because genetic defects in the ribosome machinery often leads to hematopoietic disease [11]
54 and direct quantification of ribosome location, number and conformational states in hematopoietic cells could lead
55 to new insight into hematopoietic disease [12]. To increase the amount of collected data and to provide unbiased
56 sampling of the whole lamella, we devised a new data-acquisition scheme, “Defocus-Corrected Large Area Cryo-
57 Electron microscopy” (DeCo-LACE). 2DTM allows us to test whether aberrations caused by large beam-image

shifts and highly condensed beams deteriorate the high-resolution signal. We find that these aberrations do not impede LSU detection by 2DTM. The resulting data provide a description of ribosome distribution in an entire lamella, which represent 1-2% of the cellular volume. We find a highly heterogeneous density of ribosomes within the cell. Analysis of the throughput in this method suggests that for the foreseeable future computation will be the bottleneck for visual proteomics.

Results

2DTM detects large ribosomal subunits in cryo-FIB lamellae of mammalian cells

To test whether we could detect individual ribosomes in mammalian cells we prepared cryo-lamellae of mouse neutrophil-like cells. An overview image of a representative lamella clearly shows cellular features consistent with a neutrophil-like phenotype, mainly a segmented nucleus and a plethora of membrane-organelles, corresponding to the granules and secretory vesicles of neutrophils (Fig. [1]A). We then proceeded to acquire micrographs on this lamella with a defocus of 0.5-1.0 m, $30 \text{ e}^-/\text{\AA}^2/\text{s}$ exposure and 1.76 Å pixel size. We manually selected multiple locations in the lamella and acquired micrographs using standard low-dose techniques where focusing is performed on a sacrificial area. The resulting micrographs showed smooth bilayered membranes and no signs of crystalline ice (Fig. [1]C,D), indicating successful vitrification throughout the lamella. Successful vitrification is facilitated by the small size ($\sim 8 \text{ m}$ diameter) of these cells.

We used an atomic model of the 60S mouse ribosomal subunit (6SWA) for 2DTM [13]. In a subset of images, the distribution of cross-correlation scores significantly exceeded the distribution expected from images devoid of detectable targets. In the resulting scaled maximum-intensity projections (MIPs), clear peaks with SNR values up to 10 were apparent (Fig. [2 - figure supplement 1]A). Using a threshold criterion to select significant targets (see Methods), we found that in images of cytosolic compartments there were 10-500 ribosomes within one micrograph (Fig. [1]B-E). Notably, we found no targets in areas corresponding to the nucleus (Fig. [1]B) or mitochondria (Fig. 1D). In the cytoplasm, we found a highly variable number of targets, only ~ 50 in some exposures (Fig. [1]E) and up to 500 in others (Fig. [1]C). This is a ten-fold difference in local ribosome concentration, highlighting the importance of imaging larger areas of a lamella to gain a complete picture of target distributions. We therefore set out to collect cryo-EM data for 2DTM from mammalian cell lamellae in a high-throughput unbiased fashion.

DeCo-LACE for 2D imaging of whole lamellae

In order to obtain high-resolution data from complete lamellae, we used a new approach for data collection. This approach uses three key strategies: (1) every electron that exposes a fresh area of the sample is collected on the camera (2) image shift is used to precisely and quickly raster the surface of a lamella and (3) focusing is done without using a sacrificial area (Fig. [2]A).

89 To ensure that every electron exposing a fresh area of the sample is captured by the detector, we adjusted the
90 electron beam size to be entirely contained by the detector area. During canonical low-dose imaging, the microscope
91 is configured so that the focal plane is identical to the eucentric plane of the specimen stage. This leaves the C2
92 aperture out of focus, resulting in ripples at the edge of the beam (Fig. [2]D). While these ripples are low-resolution
93 features that likely do not interfere with 2DTM [cite], we also tested data collection under conditions where the C2
94 aperture is in focus (“fringe-free”, Fig. [2]E).

95 We then centered a lamella on the optical axis of the microscope and used the image shift controls of the microscope
96 to systematically scan the whole surface of the lamella in a hexagonal pattern (Fig. [2]A,C). Instead of focusing
97 on a sacrificial area, we determined the defocus from every exposure after it was taken. The defocus was then
98 adjusted based on the difference between desired and measured defocus (Fig. [2]B). Since we used a serpentine
99 pattern for data collection, every exposure was close to the previous exposure, making large changes in the defocus
100 unlikely. Furthermore, we started our acquisition pattern on the platinum deposition edge to make sure that the
101 initial exposure where the defocus was not yet adjusted did not contain any biologically relevant information.

102 We used this strategy to collect data on eight lamellae, four using the eucentric focus condition, hereafter referred to
103 as Lamella_{EUC}, and four using the fringe-free condition, hereafter referred to as Lamella_{FFF}(Fig. [3] A+D, Fig. [4]
104 - figure supplement 4]A). We were able to collect data with a highly consistent defocus of 800 nm (Fig. [2]F), both
105 in the eucentric focus and fringe-free focus condition. To ensure that data were collected consistently, we mapped
106 defocus values as a function of the applied image shift (Fig. [3 - figure supplement 1]A). This demonstrated that
107 the defocus was consistent across a lamella, except for rare outliers and in images containing contamination. We
108 also plotted the measured objective astigmatism of each lamella and found that it varies with the applied image
109 shift, becoming more astigmatic mostly due to image shift in the x direction (Fig. [3 - figure supplement 1]B).
110 While approaches exist to correct for this during the data collection [14], we opted to not use these approaches in
111 our initial experiments. We reasoned that because 2DTM depends on high-resolution information, this would be
112 an excellent test of how much these aberration affect imaging.

113 We assembled the tile micrographs into a montage using the image-shift values and the SerialEM calibration followed
114 by cross-correlation based refinement (see Methods). In the resulting montages, the same cellular features visible
115 in the overview images are apparent (Fig. [3]B+E, Fig. [4 - figure supplement 4]B), however due to the high
116 magnification and low defocus many more details, such as the membrane bilayer separation, can be observed (Fig.
117 [3]C+F). For montages collected using the eucentric condition, there are clearly visible fringes at the edges between
118 the tiles (Fig. [3]C), which are absent in the fringe-free focus montages (Fig. [3]F). In our analysis below, we show
119 that these fringes do not impede target detection by 2DTM, making them primarily an aesthetic issue. We also
120 note that the tiling pattern is visible in the montages (Fig. [3]B+E), which we believe is due to the non-linear
121 behavior of the K3 camera since we can observe these shading artifacts in micrographs of a condensed beam over

122 vacuum (Fig. [4 - figure supplement 3]).

123 The montages show membrane vesicles and granules with highly variable sizes and density. We found that a
124 substantial number of granules, which are characterized by higher density inside the the surrounding cytosol [15],
125 seemed to contain a membrane-enclosed inclusion with density similar to the surrounding cytosol (Fig. [4 - figure
126 supplement 4]C) and could therefore be formed by an autophagy-like pathway. These granules were 150-300 nm
127 in diameter and the inclusions were 100-200 nm in diameter. Based on these dimensions the granules are either
128 azurophil or specific granules [15]. To our knowledge, these inclusion have not been described in granulocytes and
129 are further described and discussed below.

130 **2DTM of DeCo-LACE data reveals ribosome distribution in cellular cross-sections**

131 In our initial attempts of using 2DTM on micrographs acquired with the DeCo-LACE protocol, we did not observe
132 any SNR peaks above threshold using the large subunit of the mouse ribosome (Fig. [4 - figure supplement 1]A).
133 We reasoned that the edges of the beam might interfere with motion-correction of the movies as they represent
134 strong low-resolution features that do not move with the sample. When we cropped the movie frames to exclude the
135 beam edges, the estimated amount of motion increased (Fig. [4 - figure supplement 1]B), consistent with successful
136 tracking of sample motion. Furthermore, in the motion-corrected average we could identify significant SNR peaks
137 (Fig. [4 - figure supplement 1]B), confirming to high sensitivity of 2DTM to the presents of high-resolution signal
138 preserved in the images by the motion correction. To streamline data processing, we implemented a function in
139 unblur to consider only a defined central area of a movie for estimation of sample motion, while still averaging the
140 complete movie frames (Fig. [4 - figure supplement 1]C). Using this approach, we motion-corrected all tiles in the
141 eight lamellae and found consistently total motion below 1 Å per frame (Fig. [4 - figure supplement 2] A). In some
142 lamellae we found increased motion in the lamella center, which indicates areas of variable mechanical stability
143 within FIB-milled lamellae. In some micrographs we also observed that the beam edges gave rise to artifacts in
144 the MIP and numerous false-positive detections at the edge of the illuminated area (Fig. [4 - figure supplement
145 1]D). A similar phenomenon was observed on isolated “hot” pixels in unilluminated areas. To overcome this issue
146 we implemented a function in unblur to replace dark areas in the micrograph with Gaussian noise (see Methods),
147 with mean and standard deviation matching the illuminated portion of the micrograph (Fig. [4 - figure supplement
148 1]D+E). Together, these pre-processing steps enabled us to perform 2DTM on all tiles of the eight lamellae.

149 We used the refined tile positions to calculate the positions of the detected LSUs in the lamellae (Fig. [4]A, Fig. [5]A).
150 Overlaying these positions of the lamellae montages reveal ribosome distribution throughout the FIB-milled slices
151 of individual cells. Organelles like the nucleus and mitochondria only showed sporadic targets detected with low
152 SNRs, consistent with the estimated false-positive rate of one per tile. For each detected target we also calculated
153 the Z positions from the individual estimated defocus and defocus offset for each tile. When viewed from the side,

154 the ribosome positions therefore show the slight tilts of the lamellae relative to the microscope frame of reference
155 (Fig. [4]B, Fig. [5]B). Furthermore, the side views indicated that lamellae were thinner at the leading edge. Indeed,
156 when plotting the transmitted beam intensities in individual tiles as a function of beam image-shift, we observed
157 substantially higher intensities at the leading edge (Fig. [4 - figure supplement 2]B), which in energy-filtered TEM
158 indicates a thinner sample [16]. Even though we prepared the lamellae with the “overtilt” approach [17], this means
159 that ribosome densities across the lamellae can be skewed by a change in thickness, and better sample preparation
160 methods are needed to generate more even samples.

161 Close inspection of the ribosome positions in the lamellae revealed several interesting features. Ribosomes could
162 be seen associating with membranes, in patterns reminiscent of the rough endoplasmic reticulum (Fig. [4]C, Fig.
163 [5]C) or the outer nuclear membrane (Fig. [4]D). We also observed ribosomes forming ring-like structures (Fig.
164 [4]E), potentially indicating circularized mRNAs [18]. While ribosomes were for the most part excluded from the
165 numerous granules observed in the cytoplasm, in some cases we observed clusters of ribosomes in the inclusions of
166 double-membraned granules described earlier (Fig. [4]F, Fig. [5]D,E). It is, in principle, possible that these targets
167 are situated above or below the imaged granules, since the granule positions in z cannot be determined using 2D
168 projections. However, in the case of Fig. [5]E, the detected ribosomes span the whole lamella in the z direction
169 (Fig. [5]F), while positions above or below a granule would result in ribosomes situated exclusively at the top or
170 bottom of the lamella. This conclusive evidence of ribosomes in inclusions is consistent with the earlier hypothesis
171 that the inclusions are of cytoplasmic origin.

172 Does DeCo-LACE induce aberrations that affect 2DTM?

173 Within the eight lamellae we found different number of detected targets (Fig. [6]A). Lamella_{EUC} 1 had the most
174 detected targets, but also has the largest surface area and contained cytoplasm from two cells. Lamella_{FFF} 4 had
175 the fewest detected targets, but this particular lamella was dominated by a circular section of the nucleus, with only
176 small pockets of cytoplasm (Fig. [4 - figure supplement 4]). In an attempt to normalize for these differences in area
177 containing cytoplasm, we compared the number of detected targets per tile in tiles that contained more than one
178 target, which should exclude tiles with non-cytosolic content (Fig. [6]B). While this measure had less variability,
179 there were still differences. Lamella_{EUC} 4 had not only the fewest targets, but also the lowest density, which could
180 be due to this lamella being the thinnest, or due to it sectioning the cell in an area with a lower concentration of
181 ribosomes. Lamella_{FFF} 3 had a substantially higher number of ribosomes per tile. Since all of these lamellae were
182 made from a cell-line under identical conditions, this underscores the necessity to collect data from large numbers
183 of lamellae to overcome the inherent variability. When comparing the distribution of scores between lamellae, we
184 found them to be fairly comparable with median SNRs ranging from 8.7 to 9.7 (Fig. [6]C). Lamella_{EUC} 1 had
185 slightly lower scores compared to the rest, potentially due to its large size and connected mechanical instability
186 during imaging. Overall, we did not observe differences in the number or SNR of detected targets between eucentric

187 or fringe-free illumination conditions that were bigger than the observed inter-lamella variability.
188 Since the SNR values of 2DTM are highly sensitive to image quality, we reasoned we could use them to verify
189 that DeCo-LACE does not introduce a systematic loss of image quality. We considered non-parallel illumination
190 introduced by the unusually condensed beam and uncharacterized aberrations near the beam periphery. When
191 plotting the SNR values of detected targets in all eight lamellae as a function of their location in the tiles, we found
192 uniformly high SNR values throughout the illuminated areas for both eucentric and fringe-free focus illumination,
193 demonstrating that both illumination schemes are suitable for DeCo-LACE (Fig. [6]D).

194 We also wondered whether large image shifts would lead aberration due to astigmatism or beam tilt [14]. We
195 reasoned that if that was the case the number of detected targets should be highest in the center of the lamella
196 where the applied beam image-shift is 0. Instead we observed that in both eucentric and fringe-free focus conditions
197 more targets were detected at the “back” edge of the lamella (Fig. [6]E). This may be due to the center of the
198 cell being predominantly occupied by the nucleus, despite its segmentation in neutrophil-like cells. The increase in
199 matches at the “back” of the lamellae compared to the “front” can also be explained by the thickness gradient of the
200 lamellae (Fig. [4 - figure supplement 2]B, Fig. [4]B, Fig. [5]B). In addition, aberrations would be expected to cause
201 average 2DTM SNRs to be higher when beam-image shift values are small. Instead, we found that SNRs were
202 on average the highest at the “front” edge of the lamellae, presumably due to the thinner sample. We therefore
203 conclude that factors other than beam image-shift or beam condensation aberrations are limiting 2DTM SNRs,
204 predominantly the thickness of the lamellae.

205 Computation is the bottleneck of visual proteomics

206 As described above, the variability of lamellae, both in terms of experimental parameters including area, thickness
207 and mechanical stability, and in terms of biology, such as selection of cell type and location of the section within the
208 cell, requires collection of orders of magnitude more data than in this study to draw quantitative and statistically
209 relevant conclusions about the number and location of molecules under different experimental conditions. The
210 samples used were prepared in two 24 h sessions on a FIB/SEM instrument, and imaging was performed during
211 another two 24h session on the TEM microscope. Inspections of the timestamps of the raw data files revealed that
212 the milling time per lamella was ~30 minutes and TEM imaging was accomplished in ~10 seconds per tile or 90
213 minutes for a ~ 6x6 m lamella. Processing of the data, however, took substantially longer. Specifically, 2DTM of
214 all tiles took approximately one week per lamella on 32 A100 GPUs. Computation is therefore a bottleneck in our
215 current workflow, and further optimizations of the algorithm may be necessary increase throughput. Alternatively,
216 this bottleneck could be reduced by increasing the number of processing units.

217 **Discussion**

218 In this study we developed an approach to image entire cellular cross-section using cryo-EM at high enough resolution
219 to allow for 2DTM detection of the LSU. The two main advantages compared to previous approaches are a high
220 throughput of imaging and the biological context for detected molecules. The requirement to increase throughput in
221 cryo-EM data collection of cellular samples has been recognized in the recent literature. Most approaches described
222 so far are tailored towards tomography. Peck et al. [19] and Yang et al. [20] developed approaches to increase the
223 FOV of tomogram data-collection by using a montaging technique. Peck et al. used a similar “condensed-beam”
224 approach as described here. However, the montages are substantially smaller in scope, covering carbon film holes
225 of 2 um diameter. Bouvette et al. [21] and Eisenstein et al. [22] are using beam image-shift to collect tilt-series in
226 multiple locations in parallel to increase throughput. However, none of these approaches provide the full coverage
227 of a cellular cross-section that can be achieved using DeCo-Lace.

228 Since we observed substantial variation in ribosome density within and between lamellae, visual proteomics studies
229 that use cryo-EM to establish changes in molecular organization within cells will require orders of magnitude more
230 data than used in this study. One milestone would be to image enough data to represent one cellular volume, which
231 for a small eukaryotic cells requires imaging approximately 100 lamella. While data collection throughput on the
232 TEM is fundamentally limited by the exposure time, this amount of data could be collected within 12 hour by
233 improving the data acquisition scheme to perform all necessary calculation in parallel with actual exposure of the
234 camera. Sample preparation using a FIB/SEM is also currently a bottleneck, but preparation of large lamellae with
235 multiple cellular cross-sections using methods like WAFFLE [23] might allow sufficient throughput. As stated in
236 the results, at least for 2DTM computation will remain challenging and approximately 17,000 GPU hours would
237 be required for a 100 lamellae dataset.

238 As described in [7] the 2DTM SNR threshold for detecting a target is chosen to result in one false positive detection
239 per image searched. We would therefore expect to find one false positive detection per tile. We reasoned that the
240 large nuclear area imaged by DeCo-Lace could be used to test whether this assumption is true. In the 670 tiles
241 containing exclusively nucleus (as manually annotated from the overview image) we detected 247 targets, making
242 the false-positive rate more than twofold lower than expected. Since earlier work shows that 2DTM with the LSU
243 can produce matches to nuclear ribosome biogenesis intermediates [24], this could even be an overestimate of the
244 false-positive rate. This suggests that the detection threshold could be even lower, which is an area of ongoing
245 research.

246 We found that even though we used beam image-shift extensively (up to 7 um), we did not see substantially reduced
247 2DTM SNR values in tiles acquired at high beam image-shift compared to tiles acquired with low or no beam image-
248 shift. This is in contrast to reports in single-particle analysis (SPA) [25] where the induced beam tilt substantially
249 reduced the resolution if it was not corrected during processing. It is possible that 2DTM is less sensitive to beam-

250 tilt aberrations, since the template is free of any aberration and only the image is distorted, while in SPA the beam
251 tilt will affect both the images and the reconstructed template.

252 As mentioned in the results, we found a consistent shading artifact pattern in our montages, that we believe is the
253 result of non-linear behavior of the K3 camera. Indeed, when we average images with a condensed beam taken
254 over vacuum we found in both focus conditions a consistent background pattern with a brighter region on the
255 periphery of the illuminated area (Fig [4 - figure supplement 3]). This might be caused by dynamic adjustment
256 of the internal camera counting threshold which expects columns of the sensor to be evenly illuminated as is the
257 case for SPA applications. Since the signal of this pattern has mainly low-resolution components it is unlikely to
258 affect 2DTM. However, it highlights that the non-linear behavior of the camera has to be taken into account when
259 imaging samples with strongly varying density and unusual illumination schemes.

260 Unexpectedly, we observed granules containing a vesicle of putative cytosolic origin. We speculate that upon
261 degranulation, the process in which granules fuse with the plasma membrane, these vesicles would be released
262 into the extracellular space. The main types of extracellular vesicles of this size are exosomes, up to 100 nm
263 large vesicles derived from fusion of multivesicular bodies with the plasma membrane, and microvesicles, which are
264 derived from direct budding of the plasma membrane [26]. We suggest that granulocytes could release a third type
265 of extracellular vesicle, granule-derived vesicles (GDV), into the extracellular space. 2DTM showed that a subset
266 of GDVs can contain ribosomes (Fig. [4]F, Fig. [5]D,E). This could indicate that these vesicles are transporting
267 translation-capable mRNAs, as has been described for exosomes [27]. Further studies will be necessary to confirm
268 the existence of GDVs in granulocytes isolated from mammals and to understand their functional significance.

269 Materials and Methods

270 Grid preparation

271 ER-HoxA9 cells were maintained in RPMI medium supplemented with 10% FBS, penicillin/streptomycin, SCF,
272 and estrogen [10] at 37 °C and 5% CO₂. 120 h prior to grid preparation, cells were washed twice in PBS and
273 cultured in the same medium except without estrogen. Differentiation was verified by staining with Hoechst-dye
274 and inspection of nuclear morphology. Cells were then counted and diluted to $1 \cdot 10^6$ cells/ml. Grids (either 200
275 mesh copper grids, with a silicone-oxide and 2 μm holes with a 2 μm spacing or 200 mesh gold grids with a thin
276 gold film and 2 μm holes in 2 μm spacing) were glow-discharged from both sides using a 15 mA for 45 s. 3.5 μl
277 of cell suspension was added to grids on the thin-film side and grids were blotted from the back side using a GP2
278 cryoplunger (Leica) for 8 s and rapidly plunged into liquid ethane at -185 °C.

279 **FIB-milling**

280 Grids were loaded into an Aquilos 2 FIB/SEM (Thermo Fisher) instrument with a stage cooled to -190 °C. Grids
281 were sputter-coated with platinum for 15 s at 45 mA and then coated with a layer of platinum-precursor by opening
282 the GIS-valve for 45 s. An overview of the grid was created by montaging SEM images and isolated cells at the
283 center of gridsquares were selected for FIB-milling. Lamellae were generated automatically using the AutoTEM
284 software (Thermo Fisher), with the following parameters:

- 285 • Milling angle: 20°
286 • Rough milling: 3.2 μm thickness, 0.5 nA current
287 • Medium milling: 1.8 μm thickness, 0.3 nA current, 1.0° overtilt
288 • Fine milling: 1.0 μm thickness, 0.1 nA current, 0.5° overtilt
289 • Finer milling: 700 nm thickness, 0.1 nA current, 0.2° overtilt
290 • Polish 1: 450 nm thickness, 50 pA current
291 • Polish 2: 200 nm thickness, 30 pA current

292 This resulted in 6-10 μm wide lamella with 150-250 nm thickness as determined by FIB-imaging of the lamella
293 edges.

294 **Data collection**

295 Grids were loaded into a Titan Krios TEM (Thermo Fisher) operated at 300 keV and equipped with a BioQuantum
296 energy filter (Gatan) and K3 camera (Gatan). The microscope was aligned using a cross-grating grid on the stage.
297 Prior to each session, we carefully performed the “Image/Beam” calibration in nanoprobe. We set the magnification
298 to a pixel size of 1.76 Å and condensed the beam to ~ 900 nm diameter, resulting in the beam being completely
299 visible on the camera. To establish fringe-free conditions, the “Fine eucentric” procedure of SerialEM [28] was used
300 to move a square of the cross-grating grid to the eucentric position of the microscope. The effective defocus was
301 then set to 2 μm, using the “autofocus” routine of SerialEM. The objective focus of the microscope was changed
302 until no fringes were visible. The stage was then moved in Z until images had an apparent defocus of 2 μm. The
303 difference in stage Z-position between the eucentric and fringe-free conditions was used to move other areas into
304 fringe-free condition.

305 Low magnification montages were used to find lamellae and lamellae that were sufficiently thin and free of con-
306 tamination were selected for automated data collection. Overview images of each lamella were taken at 2250x
307 magnification (38 Å pixel size). The corners of the lamella in the overview image were manually annotated in
308 SerialEM and translated into beam image-shift values using SerialEM’s calibration. A hexagonal pattern of beam
309 image-shift positions was calculated that covered the area between the four corners in a serpentine way, with a
310 $\sqrt{3} \cdot 425$ nm horizontal spacing and $3/4 \cdot 850$ nm vertical spacing. Exposures were taken at each position with a 30

311 $e^-/\text{\AA}^2$ total dose. After each exposure, the defocus was estimated using the ctffind function of SerialEM and the
312 focus for the next exposure was corrected by the difference between the estimated focus and the desired defocus of
313 800 nm. Furthermore, after each exposure the deviation of the beam from the center of the camera was measured
314 and corrected using the “CenterBeamFromImage” command of SerialEM.

315 After data collection, a 20 s exposure at 2250x magnification of the lamella at 200 m defocus was taken for
316 visualization purposes. A Python script implementing this procedure is available at [Link to repo].

317 DeCo-LACE data processing

318 An overview of the data analysis pipeline is shown in Fig. 7.

319 **Pre-processing** Motion-correction, dose weighting and other preprocessing as detailed below was performed
320 using *cisTEM* [29]. To avoid influence of the beam-edge on motion-correction, only a quarter of the movie in the
321 center of the camera was considered for calculation of the estimated motion. After movie frames were aligned and
322 summed, a mask for the illuminated area was calculated by lowpass filtering the image with a 100 Å resolution
323 cutoff, thresholding the image at 10% of the maximal value and then lowpass filtering the mask again with a 100 Å
324 resolution cutoff to smooth the mask edges. This mask was then used to select dark areas in the image and fill the
325 pixels with Gaussian noise, with the same mean and standard deviation as the illuminated area. A custom version
326 of the unblur program [30] implementing this procedure is available at [link to decolace branch]. During motion
327 correction images were resampled to a pixel size of 1.5 Å. The contrast-transfer function (CTF) was estimated using
328 ctffind [31], searching between 0.2 and 2 m defocus.

329 **2DTM** The search template was generated from the atomic model of the mouse LSU (PDB 6SWA, exluding the
330 Epb1 subunit) using the cryo-EM simulator implemented in *cisTEM* [32]. The match_template program [9] was
331 used to search for this template in the movie-aligned, exposure-filtered and masked images, using a 1.5° angular
332 step in out-of-plane angles and a 1.0° angular step in-plane. 11 defocus planes in 20 nm steps centered around the
333 ctffind-determined defocus were searched. Targets were defined as detected when their matches with the template
334 produced peaks with a singal-to-noise ratio (SNR) above a threshold of 7.75, which was chosen based on the
335 one-false-positive-per-tile criterion [7].

336 **Montage assembly** The coordinates of each tile i , \mathbf{c}_i [2D Vector in pixels] were initialized using beam image-shift
337 of the tile, \mathbf{b}_i [2D Vector in m], and the ISToCamera matrix \mathbf{IC} , as calibrated by SerialEM:

$$\mathbf{c}_i = \mathbf{IC} \cdot \mathbf{b}_i$$

338 A list of tile pairs i, j that overlap were assembled by selecting images where $|\mathbf{c}_i - \mathbf{c}_j| < D_{Beam}$. In order to calculate

339 the precise offset between tiles i and j , $\mathbf{r}_{i,j}$, we calculated the cross-correlation between the two tiles, masked to
340 the overlapping illuminated area using the scikit-image package [33] was used to calculate refined offsets . The
341 coordinates \mathbf{c}_i were then refined by a least-square minimization against $\mathbf{r}_{i,j}$:

$$\min_{\mathbf{c}} \sum_{pairs} (\mathbf{r}_{i,j} - (\mathbf{c}_i - \mathbf{c}_j))^2$$

342 using the scipy package [34]. The masked cross-correlation and the least-square minimization was repeated once
343 more to arrive at the final tile alignment.

344 The x,y coordinates of target n detected by 2DTM in the tile i , $\mathbf{m}_{n,i}^T$, was transformed into the montage frame by
345 adding the coordinate of the tile.

$$\mathbf{m}_n^M = \mathbf{m}_{n,i}^T + \mathbf{c}_i$$

346 The z coordinate of each target was calculated as the sum of the defocus offset for the target, the estimated defocus
347 of the tile, and the nominal defocus of the microscope when the tile was acquired.

348 Images were rendered using UCSF ChimeraX [35] using a custom extension to render 2DTM results available
349 at [<https://github.com/jojoelfe/tempest>]. The Python scripts used for data processing are available under
350 [https://github.com/jojoelfe/deco_lace_template_matching_manuscript].

351 Acknowledgments

352 The authors would like to thank Bronwyn Lucas, Carsten Sachse, and Chen Xue for helpful suggestions and careful
353 reading of the manuscript. Data was collected at the UMass Chan medical School CryoEM core with help by
354 Kankang song, Christna, and Chen Xue.

355 Data availability

356 Cryo-EM movies, motion-corrected images and template matching results have been deposited in EMPIAR under
357 accession code [CODE]. The custom cisTEM version is available here [] until features have been integrated into a
358 cisTEM release. The ChimeraX extension for rendering is avaibale here []. This manuscript was prepared using the
359 manubot package [@ cite] . Custom python scripts and all files nescessary for manuscript generation are available
360 here [].

361 Figures

362 References

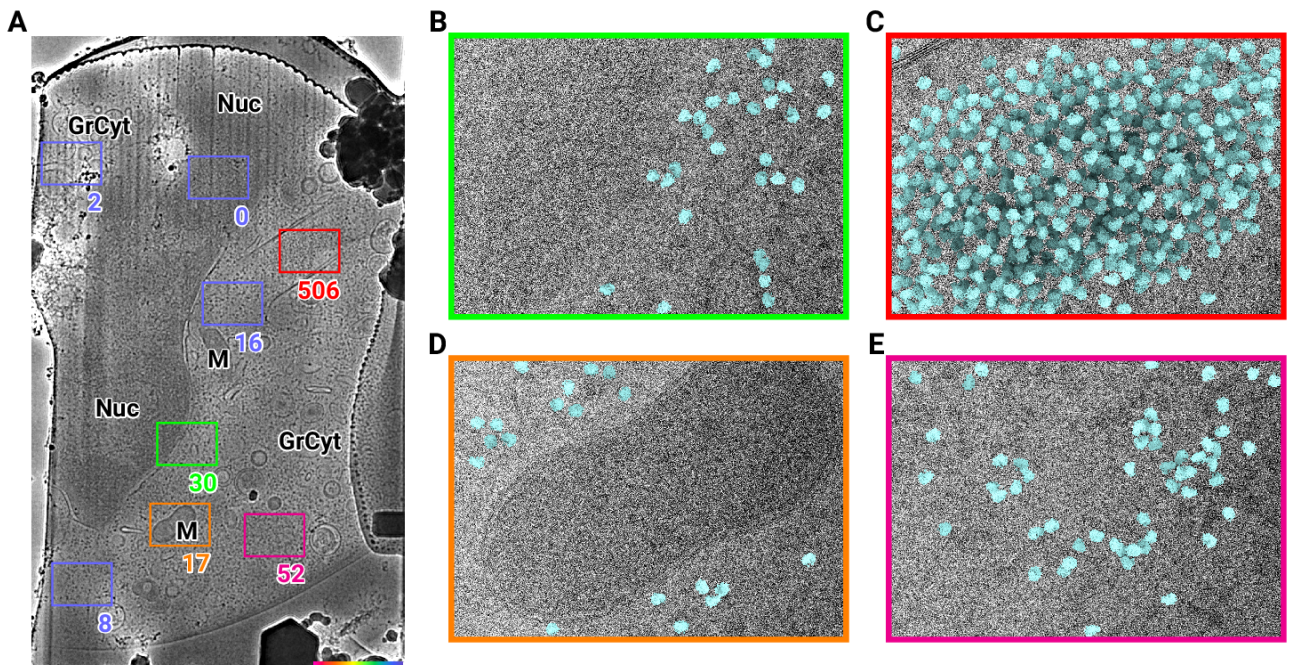


Figure 1: 2D template matching of the large subunit of the ribosome in fib-milled neutrophil-like cells (A) Overview image of the lamella. Major cellular regions are labeled, as Nucleus (Nuc), Mitochondria (M), and granular cytoplasm (GrCyt). FOVs where high-magnification images for template matching were acquired are indicated as boxes with the number of detected targets indicated on the bottom right. FOVs displayed in Panels B-E are color-coded. Scalebar corresponds to 1 m. (B-E) FOVs with projection of detected LSUs shown in cyan. (B) Perinuclear region, the only detected targets are in the cytoplasmic half. (C) Cytoplasmic region with high density of ribosomes (D) Mitochondrion, as expected there are only detected LSUs in the cytoplasmic region (E) Cytoplasm, with low density of ribosomes.

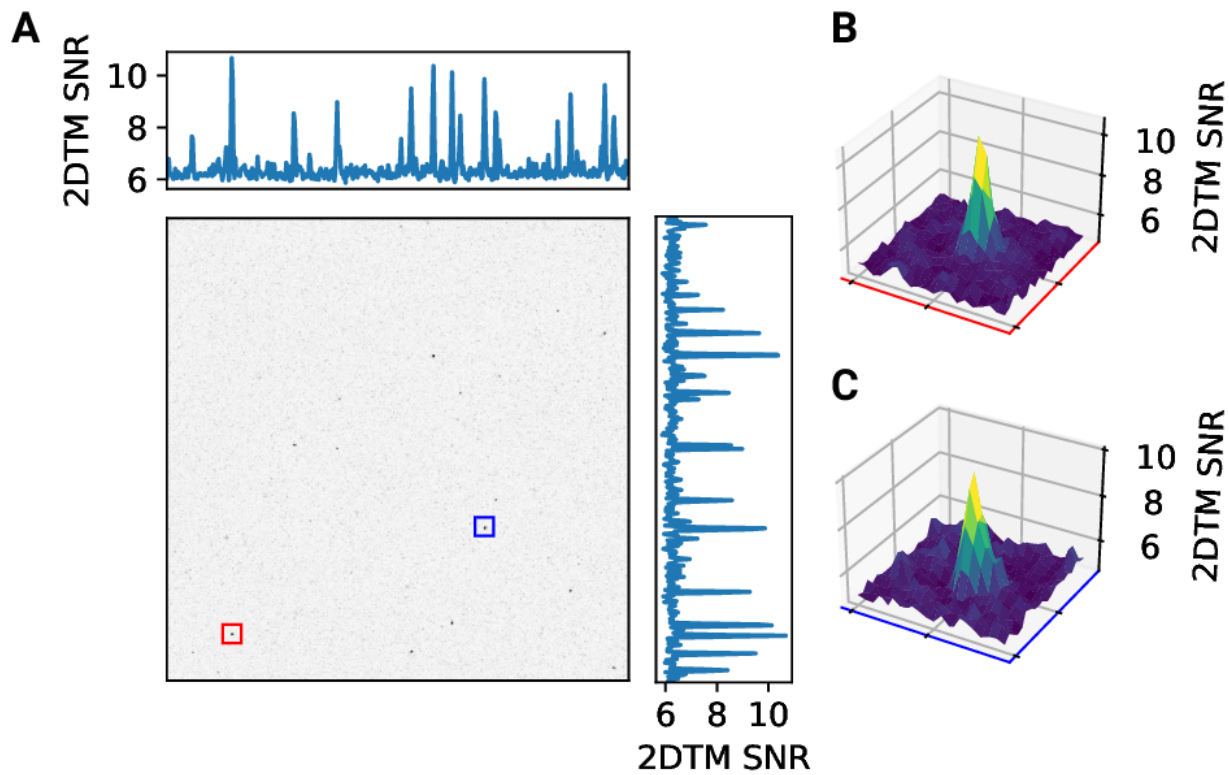


Figure 2 - figure supplement 1: 2D template matching of the large subunit of the ribosome in fib-milled neutrophil-like cells (A) Maximum intensity projection (MIP) cross-correlation map of micrograph shown in Figure 1 (B+C) 3D plot of MIP regions indicated by color boxes in Panel A

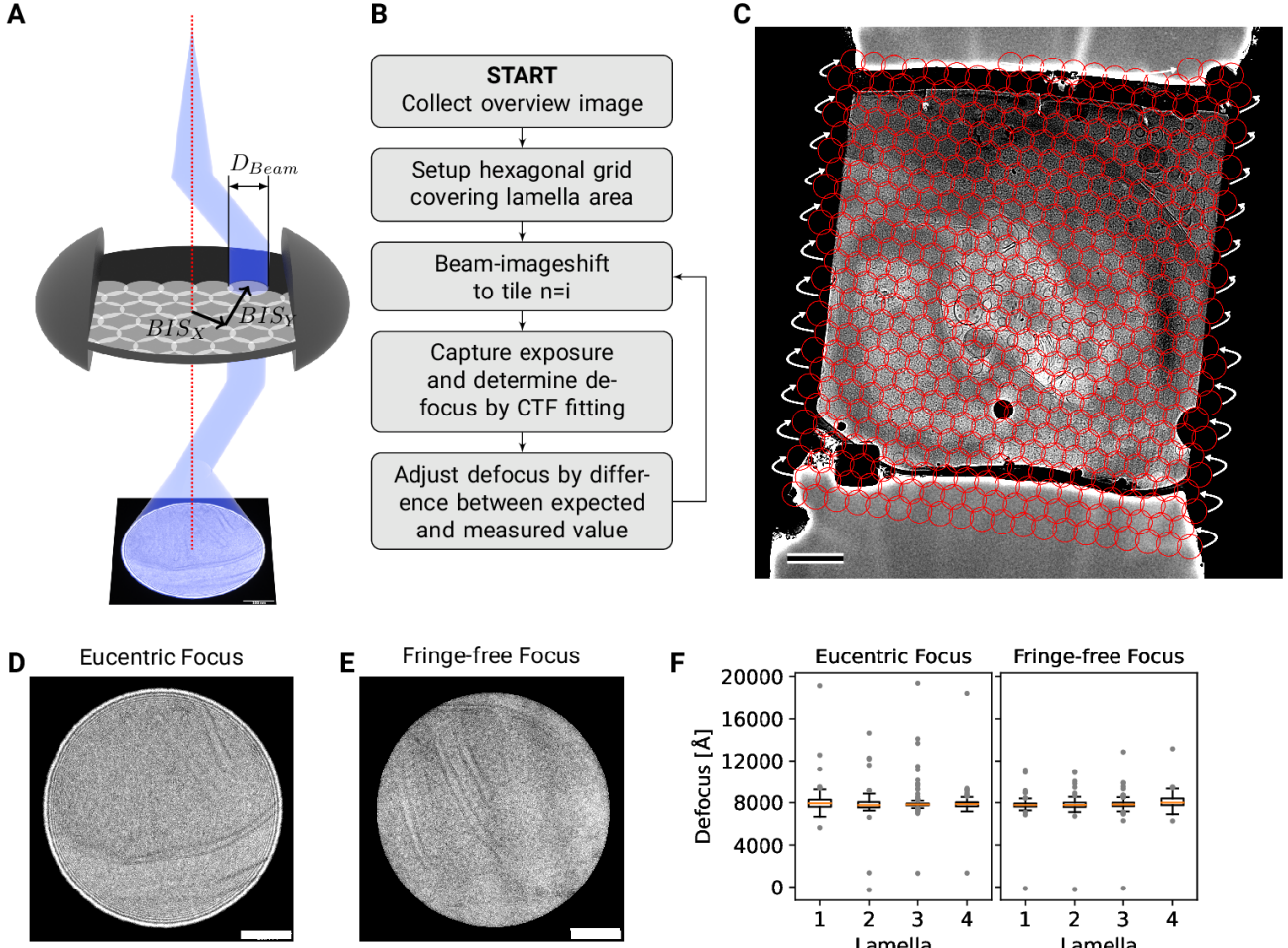


Figure 2: DeCo-LACE approach (A) Graphic demonstrating the data-collection strategy for DeCo-LACE. The electron beam is condensed to a diameter D_{Beam} that allows captured of the whole illuminated area on the camera. Beam-image shift along X and Y (BIS_X, BIS_Y) is used to scan the whole lamella (B) Diagram of the collection algorithm (C) Example overview image of a lamella with the designated acquisition positions and the used beam diameter indicated with red circles. Scalebar corresponds to 1 m. (D+E) Representative micrographs taken with a condensed beam at eucentric focus (D) or fringe-free focus (E). Scalebar corresponds to 100 nm. (F) Boxplot of defocus measured by ctffind of micrographs taken by the DeCo-Lace approach on four lamellae images at eucentric focus and four lamellae imaged with fringe-free focus.

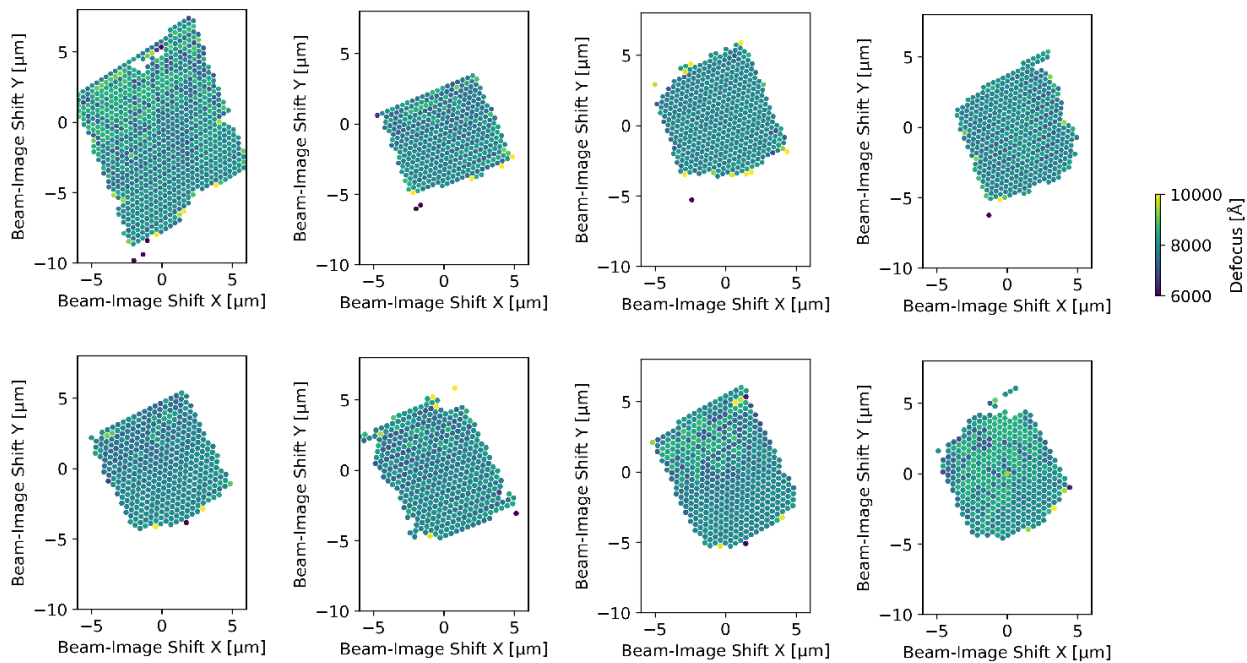
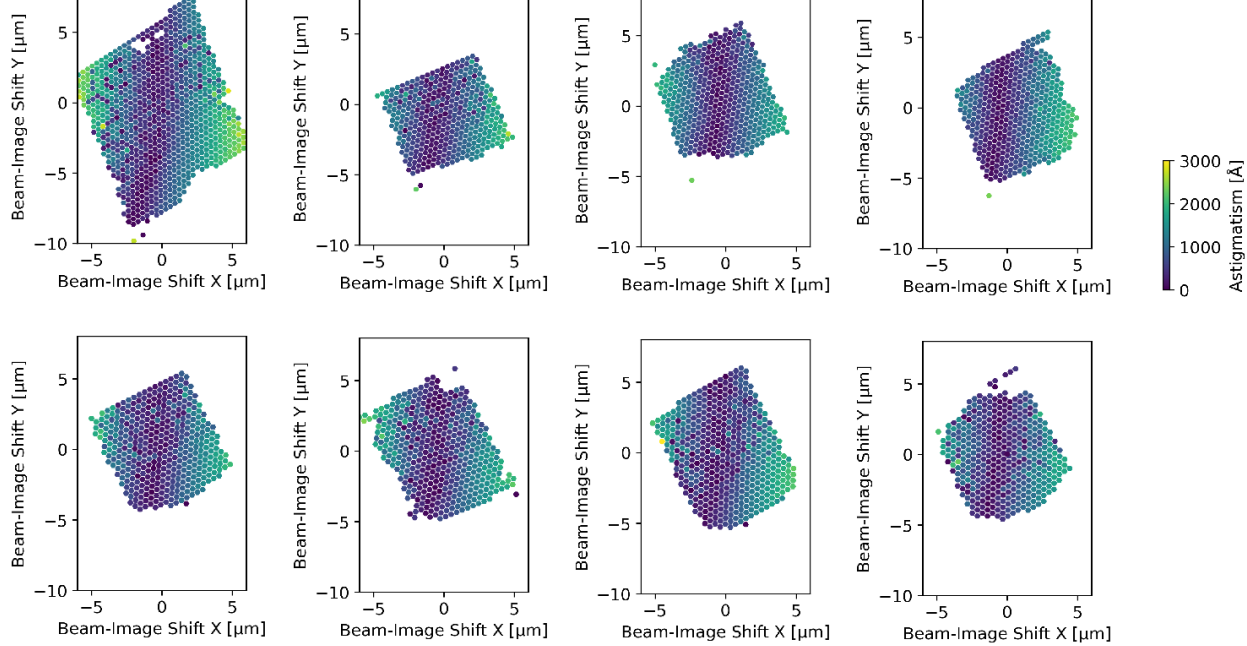
A**B**

Figure 3 - figure supplement 1: Defocus estimation of individual tiles of DeCo-Lace montages (A) Defocus values of individual micrographs taken using the DeCo-Lace approach plotted as a function of the beam image-shift values. (B) Defocus astigmatism of individual micrographs taken using the DeCo-Lace approach plotted as a function of the beam image-shift values.

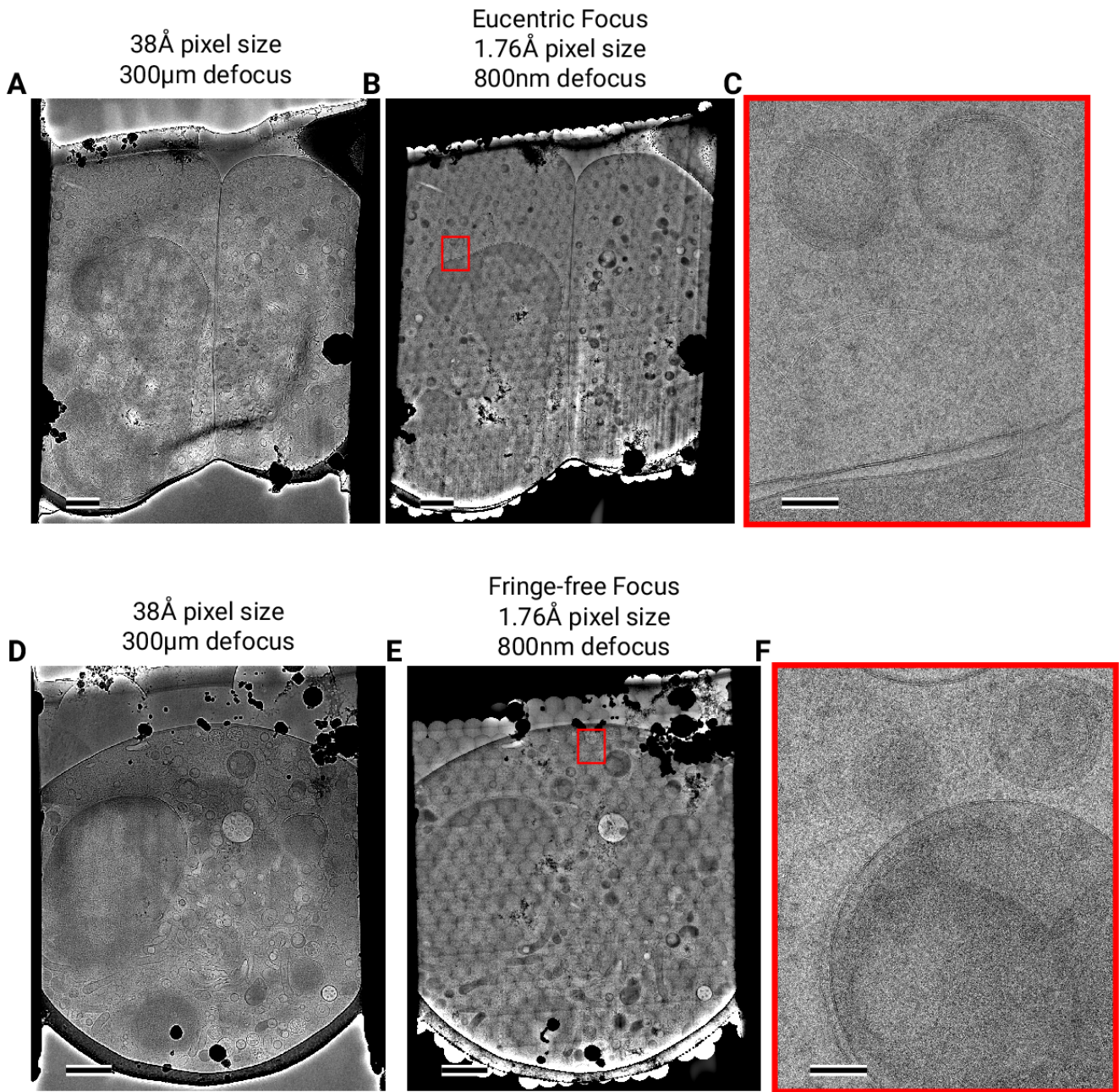


Figure 3: Assembling DeCo-LACE exposures into montages (A) Overview image of Lamella_{EUC} 1 taken at low magnification. Scalebar corresponds to 1 m. (B) Overview of Lamella_{EUC} 1 created by montaging high magnification images taken with the DeCo-Lace approach. Scalebar corresponds to 1 m. (C) Zoom-in into red box in panel B. Slight beam-fringe artifacts are visible. Scalebar corresponds to 100 nm. (D) Overview image of Lamella_{FFF} 4 taken at low magnification. Scalebar corresponds to 1 m. (E) Overview of Lamella_{FFF} 4 created by montaging high magnification images taken with the DeCo-Lace approach. Scalebar corresponds to 1 m. (F) Zoom-in into red box in panel E. No beam-fringe artifacts are visible. Scalebar corresponds to 100 nm.

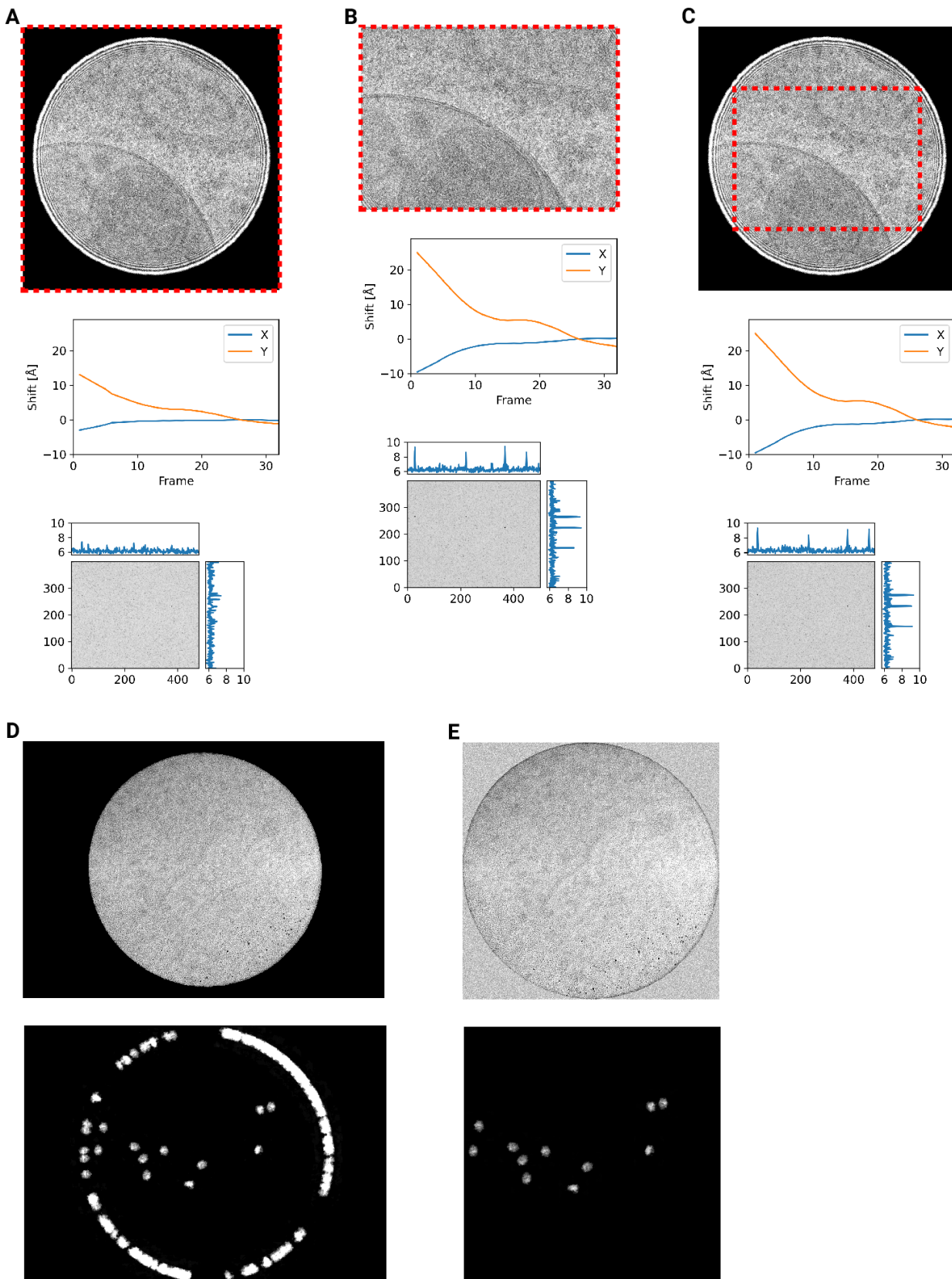


Figure 4 - figure supplement 1: Motion correction of movies with condensed beams. At the top of each panel is an average of the movie that was motion-corrected with a red dashed box indicating the region that was used to estimate shifts. Below is a graph indicating the estimated shifts of the individual frames of the movie. Below this is the MIP of 2DTM using the large subunit of the mouse ribosome. (A) Motion correction of the whole movie (B) Motion correction of a cropped region of the movie that eliminates the beam edges (C) Motion correction of the whole movie, using only the central region to estimate the shifts

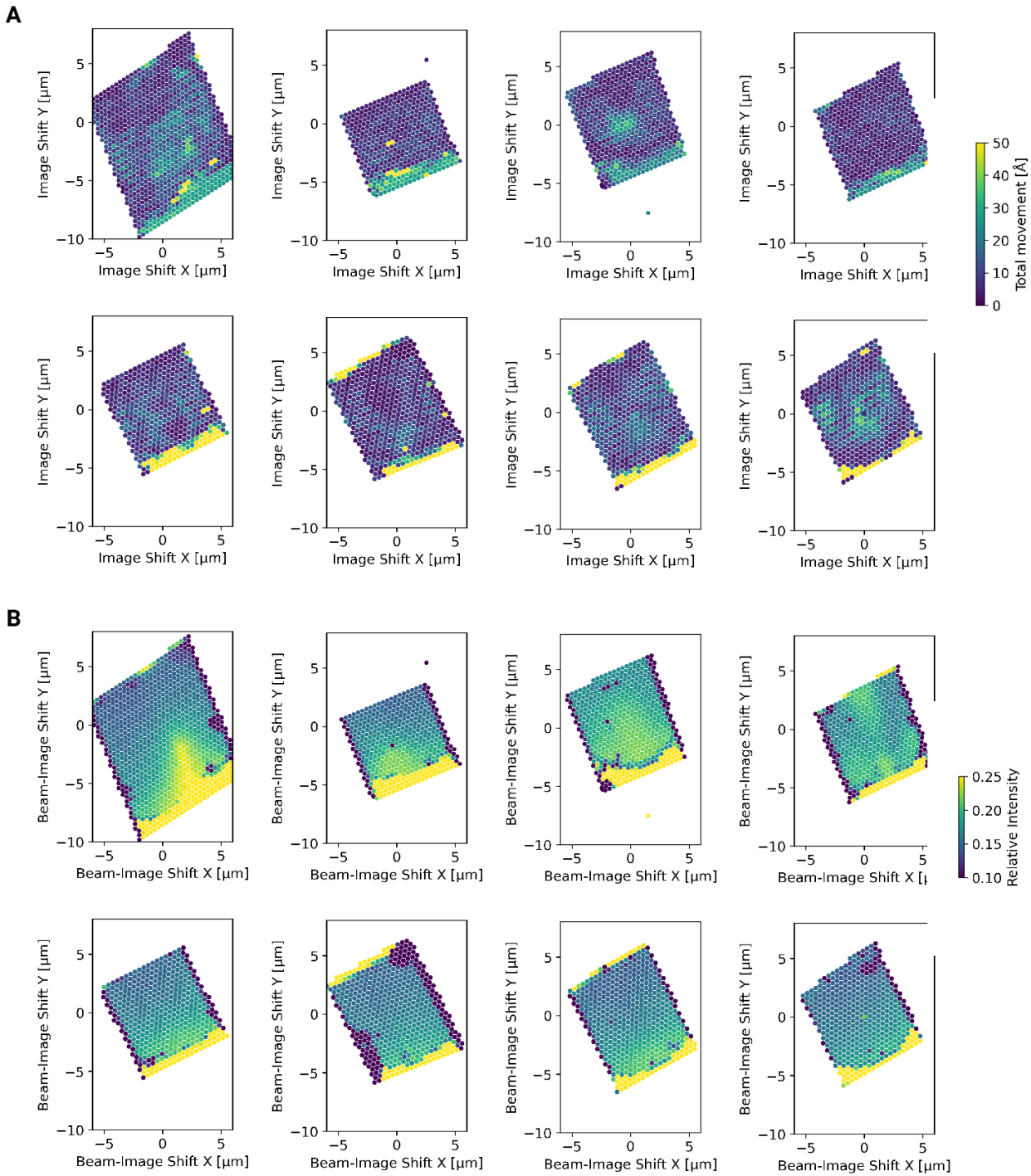


Figure 4 - figure supplement 2: Motion correction of individual tiles imaged using the DeCo-LACE approach (A) Total estimated motion of individual micrographs taken using the DeCo-Lace approach plotted as a function of the beam image-shift values. (B) Electron intensity of individual micrographs taken using the DeCo-Lace approach plotted as a function of the beam image-shift values.

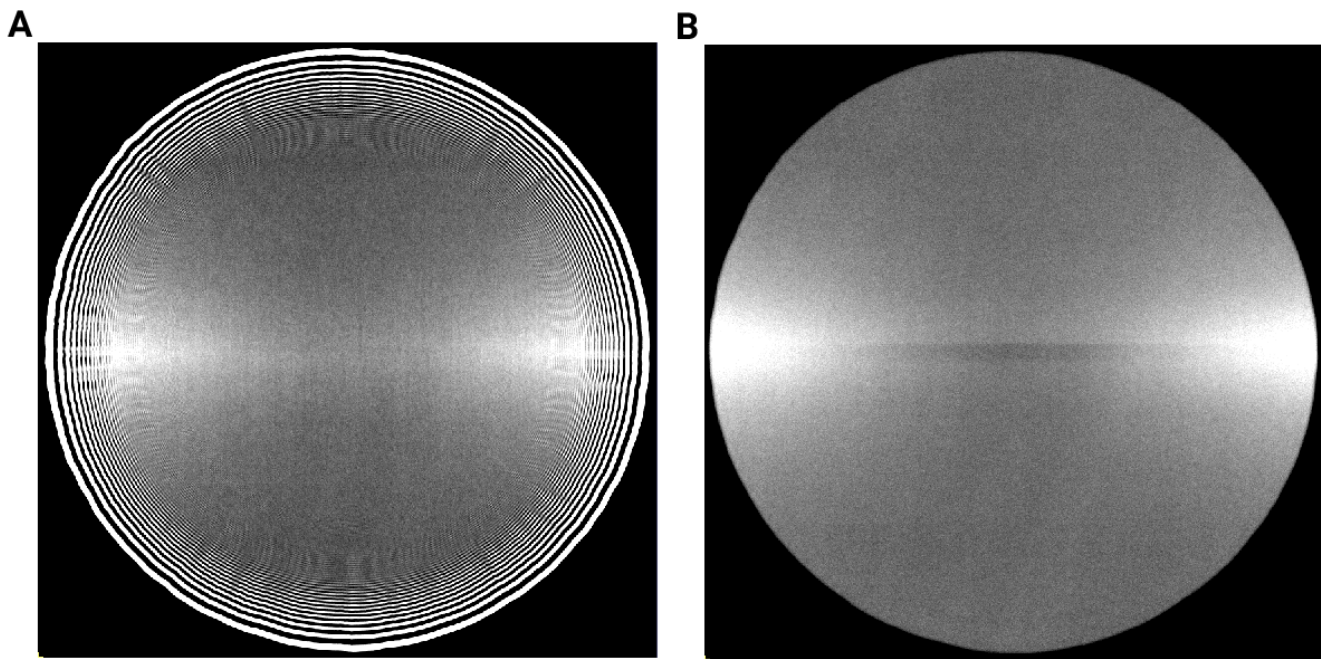


Figure 4 - figure supplement 3: Averages of micrographs taken with a condensed beam over vacuum using a Gatan K3 detector. Contrast and Brightness have been adjusted to highlight uneven dose response. (A) Eucentric Focus (B) Fringe-free Focus

363 1. **Label-free, normalized quantification of complex mass spectrometry data for proteomic analysis** Noelle M Griffin, Jingyi Yu, Fred Long, Phil Oh, Sabrina Shore, Yan Li, Jim A Koziol, Jan E Schnitzer

Nature Biotechnology (2010-01) <https://doi.org/fshgnc> DOI: 10.1038/nbt.1592 · PMID: 20010810 · PMCID: PMC2805705

364

365 2. **Fluorescence microscopy** Jeff W Lichtman, José-Angel Conchello

Nature Methods (2005-11-18) <https://doi.org/bbpg4n> DOI: 10.1038/nmeth817 · PMID: 16299476

366

367 3. **A visual approach to proteomics** Stephan Nickell, Christine Kofler, Andrew P Leis, Wolfgang Baumeister

Nature Reviews Molecular Cell Biology (2006-02-15) <https://doi.org/d6d5mq> DOI: 10.1038/nrm1861 · PMID: 16482091

368

369 4. **Electron microscopy of frozen hydrated sections of vitreous ice and vitrified biological samples** AW McDowall, J-J Chang, R Freeman, J Lepault, CA Walter, J Dubochet

Journal of Microscopy (1983-07) <https://doi.org/bdnzmv> DOI: 10.1111/j.1365-2818.1983.tb04225.x · PMID: 6350598

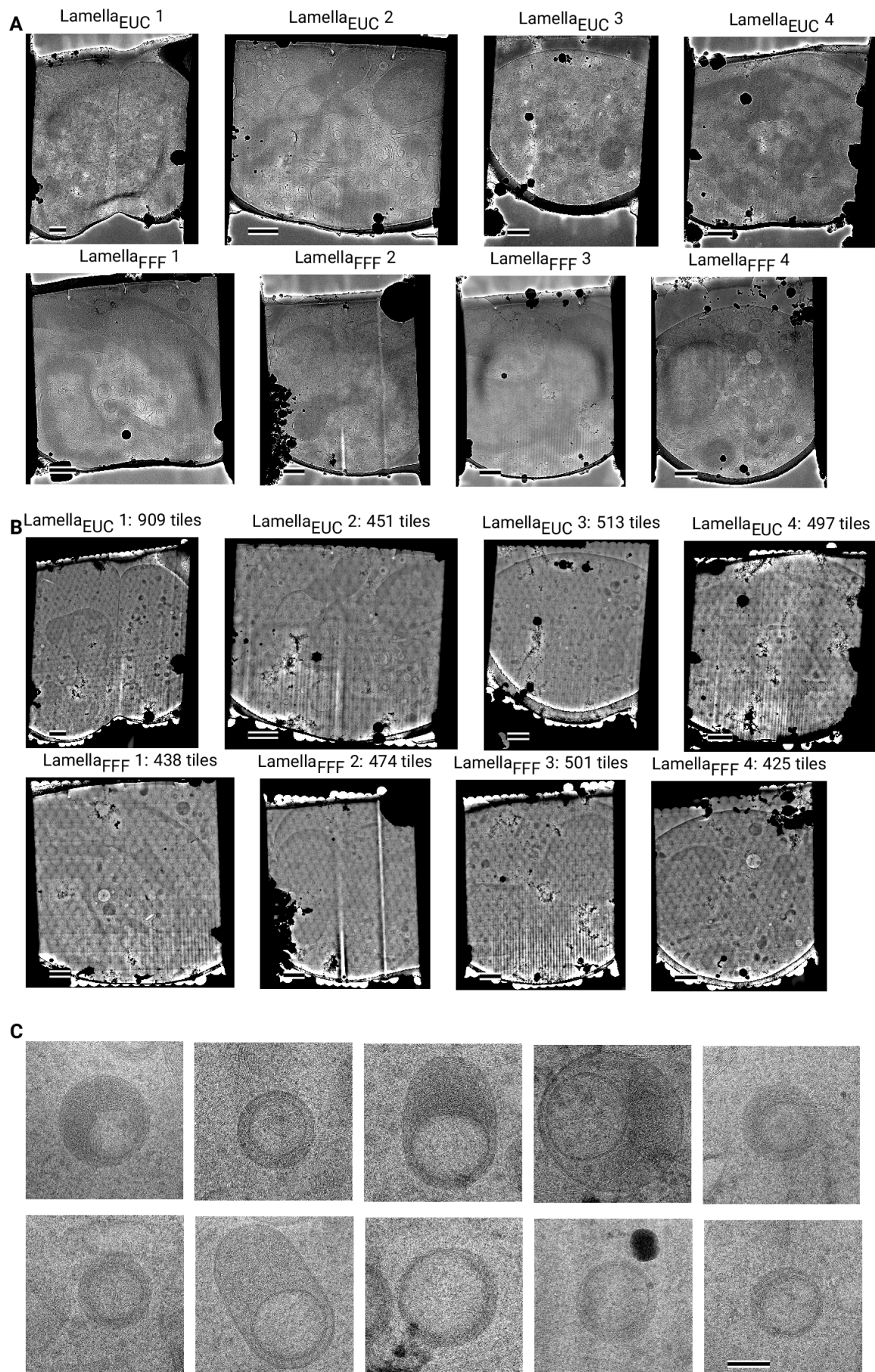


Figure 4 - figure supplement 4: Overview images of lamellae imaged using the DeCo-LACE approach taken at low-magnification (A) Overviews taken at low magnification.²¹ Scalebar corresponds to 1 m. (B) Overviews assembled using the DeCo-LACE approach. Scalebar corresponds to 1 m. (C) Representative examples of a class of granules containing a putatively cytosolic inclusion. Scalebar corresponds to 100 nm.

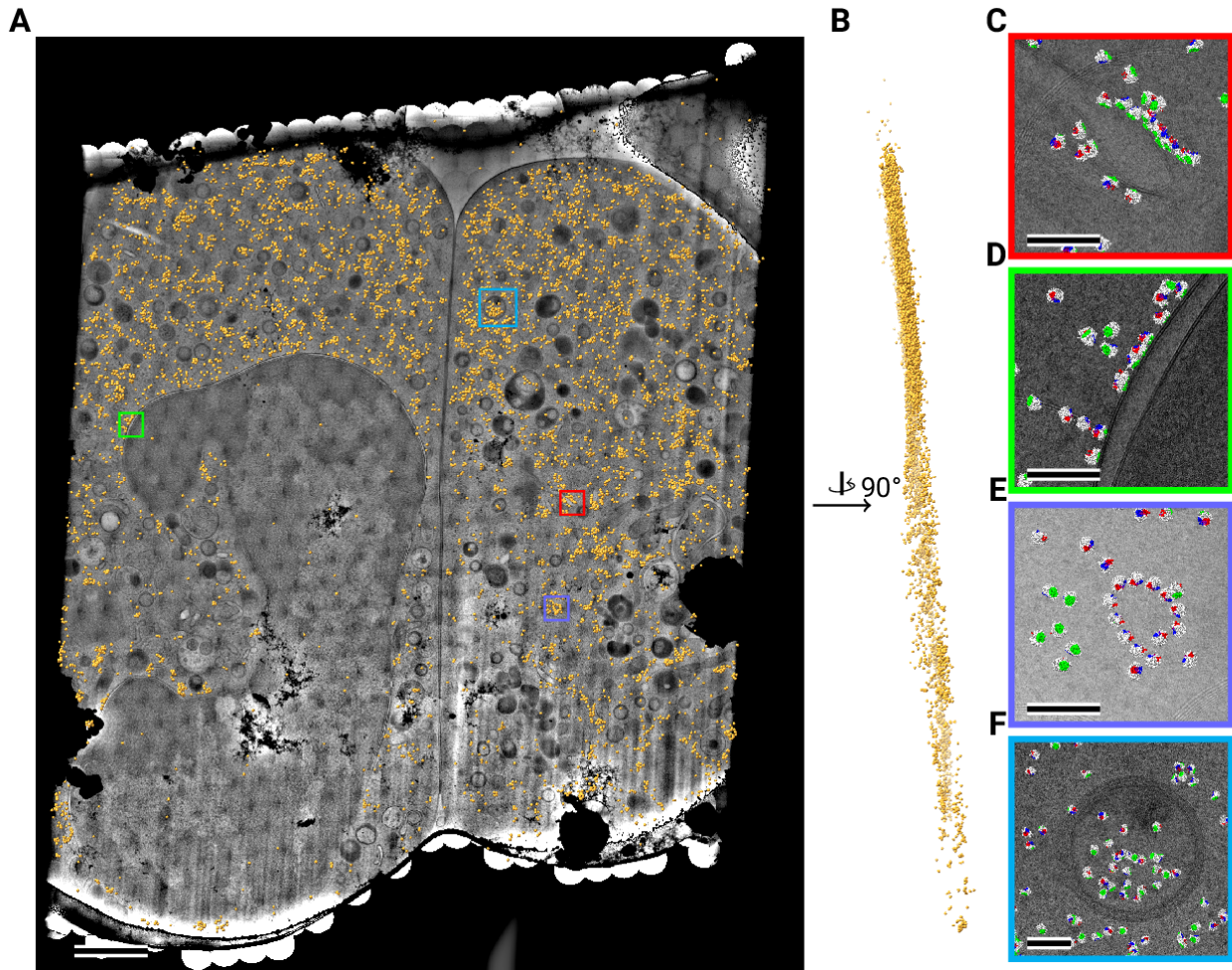


Figure 4: Template matching in lamella imaged using the DeCo-Lace approach at eucentric focus (A) Montage of Lamella_{EUC} 1 overlaid with detected targets according to their montage coordinates colored in orange. Scalebar corresponds to 1 m. (B) Side view of detected targets in the lamella, such that the direction of the electron beam is horizontal. (C-F) Magnified area of panel A showing rough ER with associated ribosomes(C), outer nuclear membrane with associated ribosomes (D), ribosomes arranged in a circular fashion(E), ribosomes enclosed in a less electron dense inclusion in a granule(F). Ribosomes are colored in white with the surface of the peptide exit tunnel colored in green and the A, P, and E sites colored in blue, purple, and red, respectively. Scalebar corresponds to 100 nm.

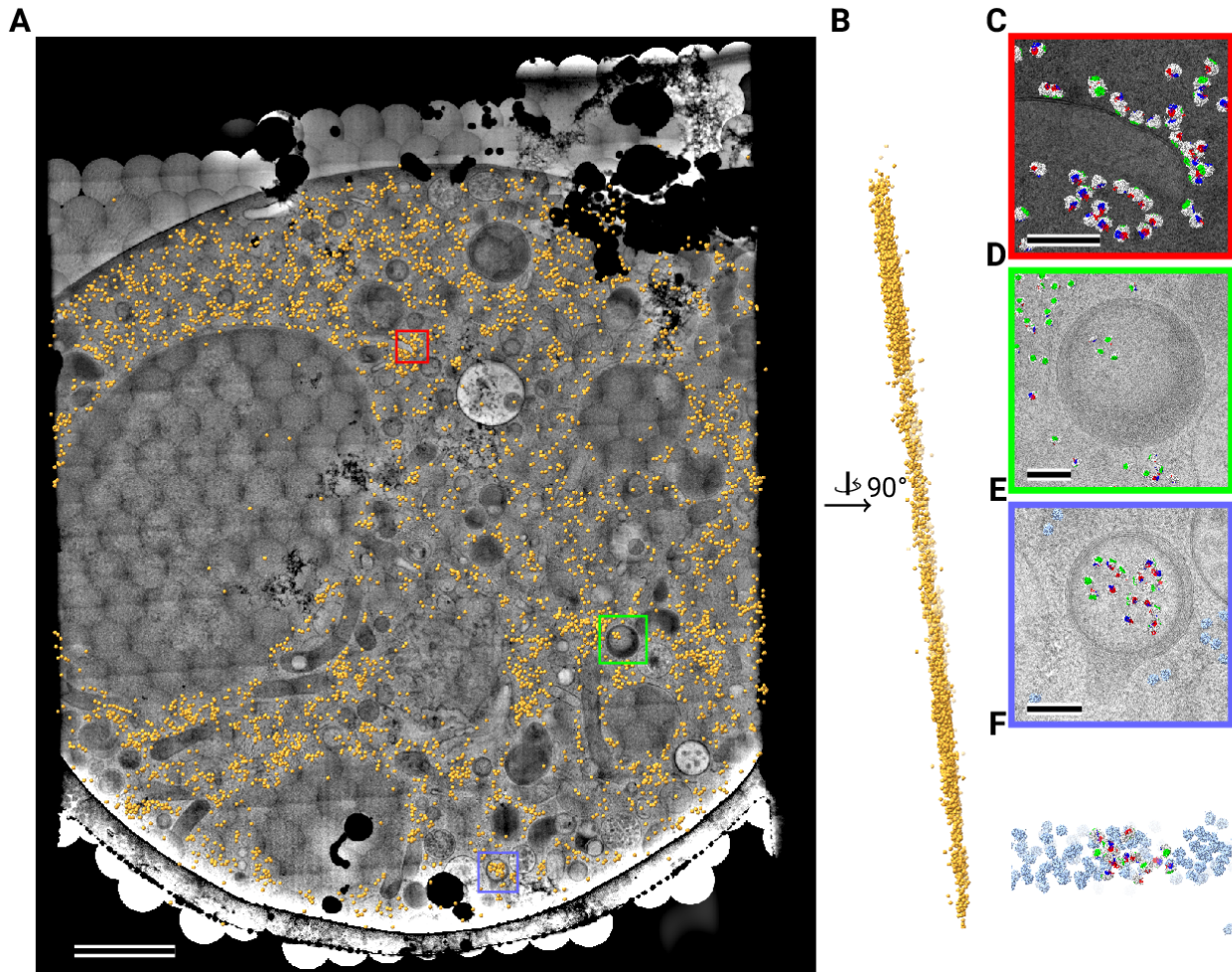


Figure 5: Template matching in lamella imaged using the DeCo-Lace approach at fringe-free focus (A) Montage of Lamella_{FFF} 4 overlaid with detected targets according to their montage coordinates colored in orange. Scalebar corresponds to 1 m. (B) Side view of detected targets in the lamella, such that the direction of the electron beam is horizontal. (C-E) Magnified area of panel A showing rough ER with associated ribosomes(C) and ribosomes enclosed in a less electron dense inclusion in a granule(D,E). (F) Side view of panel E. Ribosomes are colored in white with the surface of the peptide exit tunnel colored in green and the A, P, and E sites colored in blue, purple, and red, respectively. Scalebar corresponds to 100 nm.

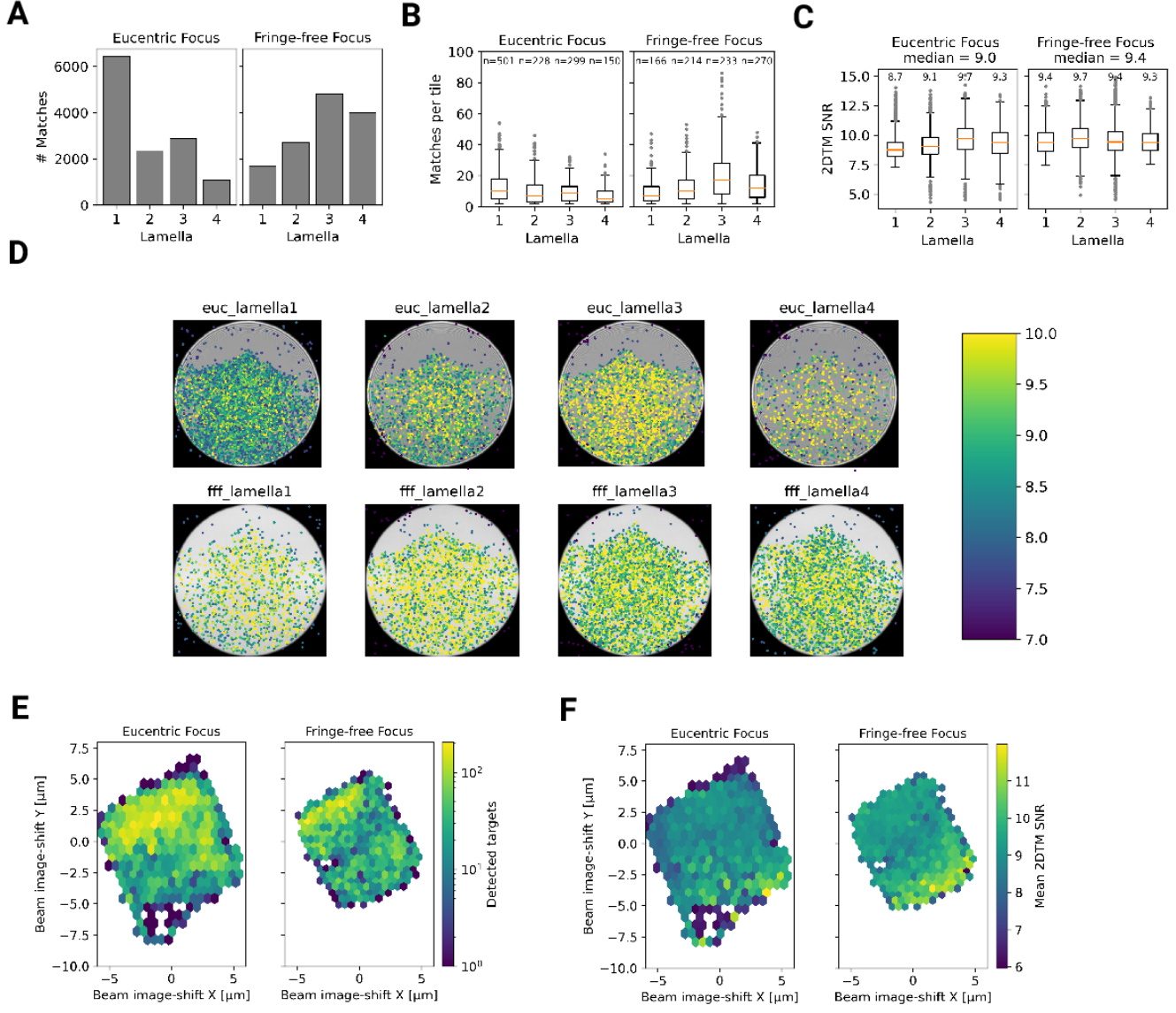


Figure 6: Statistics of 2DTM on lamella imaged using DeCo-LACE (A) Number of detected targets in each lamella (B) Distribution of targets per tile in each lamella. Only tiles with two or more detected targets were included (C) Distribution of SNRs in each lamella (D) For each lamella an average of all tiles is shown. Overlaid is a scatterplot of all detected targets in these tiles according to their in-tile coordinates. Scatterplot is colored according to the 2DTM SNR. There are no detected targets in the top circle-circle intersection due to radiation damage from previous exposures. (E) 2D histogram of number of detected targets as a function of beam-image shift (F) Mean 2DTM SNR as a function of beam-image shift

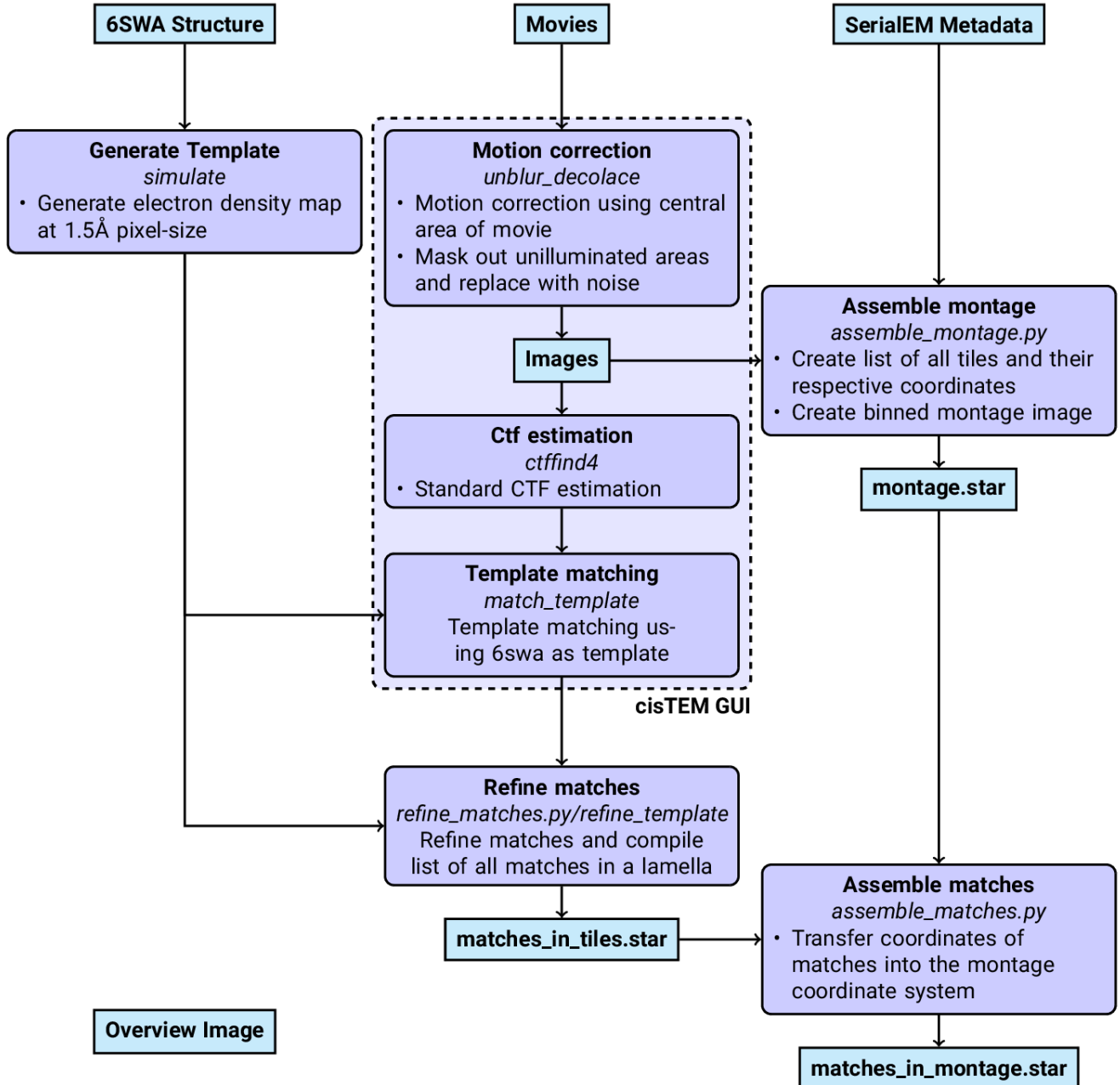


Figure 7: Workflow of DeCo-Lace processing

370

371 5. **Opening windows into the cell: focused-ion-beam milling for cryo-electron tomography**

Elizabeth Villa, Miroslava Schaffer, Jürgen M Plitzko, Wolfgang Baumeister

Current Opinion in Structural Biology (2013-10) <https://doi.org/f537jp> DOI: 10.1016/j.sbi.2013.08.006 ·

PMID: 24090931

372

373 6. **Electron tomography of cells** Lu Gan, Grant J Jensen

Quarterly Reviews of Biophysics (2011-11-15) <https://doi.org/czj9hr> DOI: 10.1017/s0033583511000102 ·

PMID: 22082691

374

375 7. **Single-protein detection in crowded molecular environments in cryo-EM images** JPeter Rick-

gauer, Nikolaus Grigorieff, Winfried Denk

eLife (2017-05-03) <https://doi.org/gnq4q4> DOI: 10.7554/elife.25648 · PMID: 28467302 · PMCID:

PMC5453696

376

377 8. **Label-free single-instance protein detection in vitrified cells** JPeter Rickgauer, Heejun Choi,

Jennifer Lippincott-Schwartz, Winfried Denk

Cold Spring Harbor Laboratory (2020-04-24) <https://doi.org/gpbjfd> DOI: 10.1101/2020.04.22.053868

378

379 9. **Locating macromolecular assemblies in cells by 2D template matching with cisTEM** Bronwyn

A Lucas, Benjamin A Himes, Liang Xue, Timothy Grant, Julia Mahamid, Nikolaus Grigorieff

eLife (2021-06-11) <https://doi.org/gkkc49> DOI: 10.7554/elife.68946 · PMID: 34114559 · PMCID:

PMC8219381

380

381 10. **Inhibition of Dihydroorotate Dehydrogenase Overcomes Differentiation Blockade in Acute**

Myeloid Leukemia David B Sykes, Youmna S Kfouri, François E Mercier, Mathias J Wawer, Jason M

Law, Mark K Haynes, Timothy A Lewis, Amir Schajnovitz, Esha Jain, Dongjun Lee, ... David T Scadden

Cell (2016-09) <https://doi.org/f3r5jr> DOI: 10.1016/j.cell.2016.08.057 · PMID: 27641501 · PMCID:

PMC7360335

382

383 11. **Hallmarks of ribosomopathies** Kim R Kampen, Sergey O Sulima, Stijn Vereecke, Kim De Keersmaecker

Nucleic Acids Research (2019-07-27) <https://doi.org/gpbjfm> DOI: 10.1093/nar/gkz637 · PMID: 31350888

· PMCID: PMC7026650

384

- 385 12. **Diagnostic and prognostic implications of ribosomal protein transcript expression patterns in**
human cancers James M Dolezal, Arie P Dash, Edward V Prochownik
BMC Cancer (2018-03-12) <https://doi.org/gc87j9> DOI: 10.1186/s12885-018-4178-z · PMID: 29530001 ·
PMCID: PMC5848553
- 386
- 387 13. **Protein Synthesis in the Developing Neocortex at Near-Atomic Resolution Reveals Ebp1-**
Mediated Neuronal Proteostasis at the 60S Tunnel Exit Matthew L Kraushar, Ferdinand Krupp,
Dermot Harnett, Paul Turko, Mateusz C Ambroziewicz, Thiemo Sprink, Koshi Imami, Manuel Gündig-
mann, Ulrike Zinnall, Carlos H Vieira-Vieira, ... Christian MT Spahn
Molecular Cell (2021-01) <https://doi.org/gh7d72> DOI: 10.1016/j.molcel.2020.11.037 · PMID: 33357414 ·
PMCID: PMC8163098
- 388
- 389 14. **High-quality, high-throughput cryo-electron microscopy data collection via beam tilt and**
astigmatism-free beam-image shift Chunling Wu, Xiaojun Huang, Jing Cheng, Dongjie Zhu, Xinzhen
Zhang
Journal of Structural Biology (2019-12) <https://doi.org/gp2nq9> DOI: 10.1016/j.jsb.2019.09.013 · PMID:
31562921
- 390
- 391 15. **THE DEVELOPMENT OF NEUTROPHILIC POLYMORPHONUCLEAR LEUKOCYTES**
IN HUMAN BONE MARROW Dorothy Ford Bainton, Joan L Ulyot, Marilyn G Farquhar
Journal of Experimental Medicine (1971-10-01) <https://doi.org/chkbcm> DOI: 10.1084/jem.134.4.907 ·
PMID: 4106490 · PMCID: PMC2138991
- 392
- 393 16. **Routine determination of ice thickness for cryo-EM grids** William J Rice, Anchi Cheng, Alex J
Noble, Edward T Eng, Laura Y Kim, Bridget Carragher, Clinton S Potter
Journal of Structural Biology (2018-10) <https://doi.org/gfbpj2> DOI: 10.1016/j.jsb.2018.06.007 · PMID:
29981485 · PMCID: PMC6119488
- 394
- 395 17. **Optimized cryo-focused ion beam sample preparation aimed at in situ structural studies of**
membrane proteins Miroslava Schaffer, Julia Mahamid, Benjamin D Engel, Tim Laugks, Wolfgang
Baumeister, Jürgen M Plitzko
Journal of Structural Biology (2017-02) <https://doi.org/f9qfr6> DOI: 10.1016/j.jsb.2016.07.010 · PMID:
27444390

- 397 18. **Circularization of mRNA by eukaryotic translation initiation factors.** SE Wells, PE Hillner, RD Vale, AB Sachs
Molecular cell (1998-07) <https://www.ncbi.nlm.nih.gov/pubmed/9702200> DOI: 10.1016/s1097-2765(00)80122-7 · PMID: 9702200
- 398
- 399 19. **Montage electron tomography of vitrified specimens** Ariana Peck, Stephen D Carter, Huanghao Mai, Songye Chen, Alister Burt, Grant J Jensen
Journal of Structural Biology (2022-06) <https://doi.org/gp4qrs> DOI: 10.1016/j.jsb.2022.107860 · PMID: 35487464
- 400
- 401 20. **Correlative cryogenic montage electron tomography for comprehensive in-situ whole-cell structural studies** Jie E Yang, Matthew R Larson, Bryan S Sibert, Joseph Y Kim, Daniel Parrell, Juan C Sanchez, Victoria Pappas, Anil Kumar, Kai Cai, Keith Thompson, Elizabeth R Wright
Cold Spring Harbor Laboratory (2022-01-02) <https://doi.org/gp4qrw> DOI: 10.1101/2021.12.31.474669
- 402
- 403 21. **Beam image-shift accelerated data acquisition for near-atomic resolution single-particle cryo-electron tomography** Jonathan Bouvette, Hsuan-Fu Liu, Xiaochen Du, Ye Zhou, Andrew P Sikkema, Juliana da Fonseca Rezende e Mello, Bradley P Klemm, Rick Huang, Roel M Schaaper, Mario J Borgnia, Alberto Bartesaghi
Nature Communications (2021-03-30) <https://doi.org/gjphkb> DOI: 10.1038/s41467-021-22251-8 · PMID: 33785757 · PMCID: PMC8009872
- 404
- 405 22. **Parallel cryo electron tomography on < i>in situ</i> lamellae** Fabian Eisenstein, Haruaki Yanagisawa, Hiroka Kashihara, Masahide Kikkawa, Sachiko Tsukita, Radostin Danev
Cold Spring Harbor Laboratory (2022-04-08) <https://doi.org/gp4qrw> DOI: 10.1101/2022.04.07.487557
- 406
- 407 23. **Waffle Method: A general and flexible approach for improving throughput in FIB-milling** Kotaro Kelley, Ashleigh M Raczkowski, Oleg Klykov, Pattana Jaroenlak, Daija Bobe, Mykhailo Kopylov, Edward T Eng, Gira Bhabha, Clinton S Potter, Bridget Carragher, Alex J Noble
Nature Communications (2022-04-06) <https://doi.org/gp4qrt> DOI: 10.1038/s41467-022-29501-3 · PMID: 35387991 · PMCID: PMC8987090

- 409 24. **< i > In situ < /i > single particle classification reveals distinct 60S maturation intermediates in**
cells Bronwyn A Lucas, Kexin Zhang, Sarah Loerch, Nikolaus Grigorieff
Cold Spring Harbor Laboratory (2022-04-10) <https://doi.org/gp4qr> DOI: 10.1101/2022.04.10.487797
- 410
- 411 25. **High-resolution cryo-EM using beam-image shift at 200 keV** Jennifer N Cash, Sarah Kearns, Yilai Li, Michael A Cianfrocco
IUCrJ (2020-10-29) <https://doi.org/gjwcf> DOI: 10.1107/s2052252520013482 · PMID: 33209328 · PMCID: PMC7642776
- 412
- 413 26. **Shedding light on the cell biology of extracellular vesicles** Guillaume van Niel, Gisela D'Angelo, Graça Raposo
Nature Reviews Molecular Cell Biology (2018-01-17) <https://doi.org/gct4df> DOI: 10.1038/nrm.2017.125 · PMID: 29339798
- 414
- 415 27. **Exosome-mediated transfer of mRNAs and microRNAs is a novel mechanism of genetic exchange between cells** Hadi Valadi, Karin Ekström, Apostolos Bossios, Margareta Sjöstrand, James J Lee, Jan O Lötvall
Nature Cell Biology (2007-05-07) <https://doi.org/d5df4s> DOI: 10.1038/ncb1596 · PMID: 17486113
- 416
- 417 28. **Automated electron microscope tomography using robust prediction of specimen movements** David N Mastronarde
Journal of Structural Biology (2005-10) <https://doi.org/ff7gzx> DOI: 10.1016/j.jsb.2005.07.007 · PMID: 16182563
- 418
- 419 29. **cisTEM, user-friendly software for single-particle image processing** Timothy Grant, Alexis Rohou, Nikolaus Grigorieff
eLife (2018-03-07) <https://doi.org/gf5cq> DOI: 10.7554/elife.35383 · PMID: 29513216 · PMCID: PMC5854467
- 420
- 421 30. **Measuring the optimal exposure for single particle cryo-EM using a 2.6 Å reconstruction of rotavirus VP6** Timothy Grant, Nikolaus Grigorieff
eLife (2015-05-29) <https://doi.org/gf5cm> DOI: 10.7554/elife.06980 · PMID: 26023829 · PMCID: PMC4471936

- 423 31. **CTFFIND4: Fast and accurate defocus estimation from electron micrographs** Alexis Rohou,
Nikolaus Grigorieff
Journal of Structural Biology (2015-11) <https://doi.org/f7xzgv> DOI: 10.1016/j.jsb.2015.08.008 · PMID:
26278980 · PMCID: PMC6760662
- 424
- 425 32. **Cryo-TEM simulations of amorphous radiation-sensitive samples using multislice wave propa-
gation** Benjamin Himes, Nikolaus Grigorieff
IUCrJ (2021-09-30) <https://doi.org/gpzs9r> DOI: 10.1107/s2052252521008538 · PMID: 34804546 · PMCID:
PMC8562658
- 426
- 427 33. **scikit-image: image processing in Python** Stéfan van der Walt, Johannes L Schönberger, Juan
Nunez-Iglesias, François Boulogne, Joshua D Warner, Neil Yager, Emmanuelle Gouillart, Tony Yu
PeerJ (2014-06-19) <https://doi.org/gftp3s> DOI: 10.7717/peerj.453 · PMID: 25024921 · PMCID:
PMC4081273
- 428
- 429 34. **SciPy 1.0: fundamental algorithms for scientific computing in Python** Pauli Virtanen, Ralf
Gommers, Travis E Oliphant, Matt Haberland, Tyler Reddy, David Cournapeau, Evgeni Burovski, Pearu
Peterson, Warren Weckesser, Jonathan Bright, ...
Nature Methods (2020-02-03) <https://doi.org/ggj45f> DOI: 10.1038/s41592-019-0686-2 · PMID: 32015543 ·
PMCID: PMC7056644
- 430
- 431 35. <scp>**UCSF ChimeraX</scp> : Structure visualization for researchers, educators, and
developers** Eric F Pettersen, Thomas D Goddard, Conrad C Huang, Elaine C Meng, Gregory S Couch,
Tristan I Croll, John H Morris, Thomas E Ferrin
Protein Science (2020-10-22) <https://doi.org/ghr6mn> DOI: 10.1002/pro.3943 · PMID: 32881101 · PMCID:
PMC7737788